A new tensorial model for suspension of non-colloidal rigid particles in Newtonian fluids

Olivier Ozenda, Pierre Saramito, Guillaume Chambon, Claude Smutek

A new tensorial model for suspension of non-colloidal rigid particles in Newtonian fluids

O. Ozenda, P. Saramito, G. Chambon and C. Smutek

May 29, 2017

1 Introduction

The suspension balance model [NB94, MM06] gives good results when compared to experimental measurements with stationary shear flows (Poiseuille and Couette). Nevertheless, it assumes a "*normal viscosity* and is restricted to shear flows. Miller and Morris [MM06] proposed a tensorial approach to introduce the normal stress components, but the proposed model it is not invariant by a change of frame and do not introduce time scales, as observed in shear reversal (see e.g. [GMA80]).

In this paper, we aim at developing an alternative model, that should be independent upon the referential, and thus suitable for more general flow situations. This model takes into account migration, frictional contacts, and anisotropic relaxation of clusters. The existence of non-zero normal stresses is here a consequence of the usage of an Oldroyd tensor derivative for the stress tensor associated to particle clusters. This tensor derivatives is associated to a characteristic time for clusters of particles to relax. This approach furnish also results in better agreement with the expected time-dependent behavior, such as simple shear [KPGM02, NSH+02] reversal and Couette reversal experiments [GMA80, Bla11]. Finally, this tensor based model should be able to better describe the experimentally observed anisotropic effects, pointed out with pair-distribution functions.

The first section presents the model statement while the second one turns to time dependent flows, specifically shear reversals. The third section present some comparison between the model prediction and several experimental measurements on stationary simple shear flows.

2 Model statement

2.1 From microscopic to macroscopic level

The tensor of deformation of particle clusters $\boldsymbol{\gamma}_e$ can defined in terms of averages of microscopic quantities: the *statistical texture tensor*, denoted as $\boldsymbol{m}$ and represented on Fig. 1.left. The concept of texture tensor already used in [AJGG03] in the context of liquid foams and extended to various applications such as anisotropic damage of the sea ice [LWD+15]. The texture tensor is defined as an average of links $\boldsymbol{\ell}$, at the microscopic level, between particles in contact, i.e. $\boldsymbol{m} = \langle \boldsymbol{\ell} \otimes \boldsymbol{\ell} \rangle$. The average, denoted by $\langle . \rangle$, is performed at an intermediate mesoscopic level called the representative volume around the current position. Then, we define the elastic strain as $\boldsymbol{\gamma}_e = -c \log(\boldsymbol{m})$ where $c > 0$ is a normalization coefficient. Note that it writes equivalently $\boldsymbol{m} = \exp(-c\boldsymbol{\gamma}_e)$. The tensor $\boldsymbol{\gamma}_e$ has the same eigenvectors as $\boldsymbol{m}$ but eigenvalues equal to the logarithm of those of $\boldsymbol{m}$. The minus sign expresses that the the largest eigenvalue of $\boldsymbol{\gamma}_e$ corresponds to the smallest of $\boldsymbol{m}$, i.e. the compression axis.

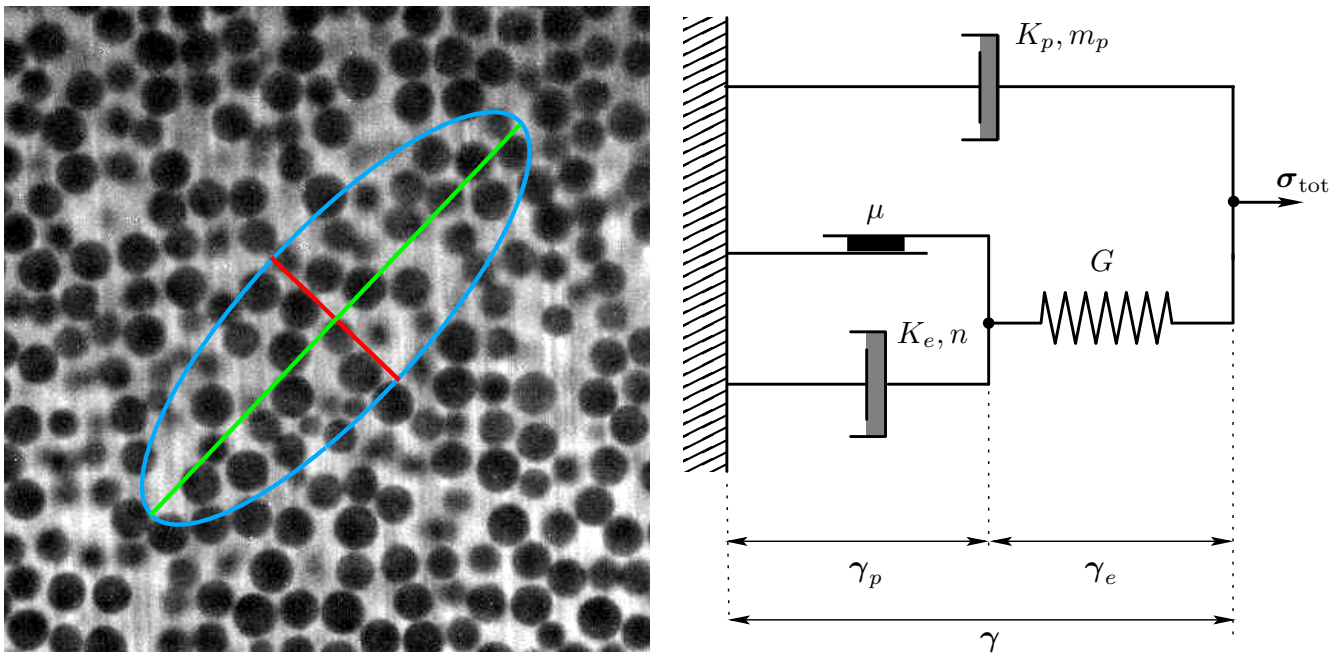

Figure 1: (left) Representation of the local particle clusters by a texture tensor $\boldsymbol{m}$. This tensor is represented by an ellipse. Its compression axis is in red and its dilatation axis in green. Background photography from [Bla11], Fig. 4.7 with $\phi = 0.55$. (right) Schematic diagram of the rheological model: link between the total stress $\boldsymbol{\sigma}_{\text{tot}}$ and the total deformation $\boldsymbol{\gamma} = \boldsymbol{\gamma}_e + \boldsymbol{\gamma}_p$.

Let $\boldsymbol{\gamma}$ denote the total deformation of the suspension. We assume that it can be decomposed as the sum of the particle cluster deformation $\boldsymbol{\gamma}_e$ and large deformations $\boldsymbol{\gamma}_p$ due to rearrangements of contacts between particles (see Fig. 1.right):

$$\boldsymbol{\gamma} = \boldsymbol{\gamma}_e + \boldsymbol{\gamma}_p \tag{1}$$

The particle stress, denoted as $\boldsymbol{\tau}$, decomposes as the sum of $\boldsymbol{\tau}_c$, the contribution due to frictions at contacts between particles, and $\boldsymbol{\tau}_h$, the contribution due to small distance hydrodynamic interaction between particles.

The deviatoric part of the particle stress due to frictions at contacts between particles is expressed by the Drucker and Prager [DP52] relation:

$$\text{dev}(\boldsymbol{\tau}_c) \quad = \quad \mu p_p \frac{\text{dev}(\dot{\boldsymbol{\gamma}}_p)}{|\text{dev}(\dot{\boldsymbol{\gamma}}_p)|}$$

where $p_p = \text{tr}(\boldsymbol{\tau})/3$ denotes the total particle pressure and $\mu \geqslant 0$ is the constant friction coefficient, related to the Coulomb friction rules at the microscopic level. The effect of friction between particles in contact as been pointed out by several experimental observations (see e.g. [BGP11]). The dot, as $\dot{\boldsymbol{\gamma}}_p$ denotes the time derivative of the deformation $\boldsymbol{\gamma}_p$ tensor. Here, $|.|$ denotes the matrix norm, defined for all matrix $\boldsymbol{\sigma}$ by

$$|\boldsymbol{\sigma}| \quad = \quad \left(\frac{\boldsymbol{\sigma} : \boldsymbol{\sigma}}{2}\right)^{1/2} \quad = \quad \left(\sum_{i,j=1}^{3} \boldsymbol{\sigma}_{i,j}\right)^{1/2}$$

where : denotes the double dot product between two matrix. The deviatoric part of the particle stress due to small distance hydrodynamic interactions between particles is expressed by a power-law rule:

$$\text{dev}(\boldsymbol{\tau}_h) \quad = \quad K_e \, |\text{dev}(\dot{\boldsymbol{\gamma}}_p)|^{-1+n} \text{dev}(\dot{\boldsymbol{\gamma}}_p)$$

where K_e is the consistence and $n > 0$ is the constant power-law index. Summing the two previous relations leads to

$$\mathrm{dev}(\boldsymbol{\tau}) \;=\; \left(K_e \,|\mathrm{dev}(\dot{\boldsymbol{\gamma}}_p)|^{-1+n} + \frac{\mu\,\mathrm{tr}(\boldsymbol{\tau})/3}{|\mathrm{dev}(\dot{\boldsymbol{\gamma}}_p)|} \right) \mathrm{dev}(\dot{\boldsymbol{\gamma}}_p)$$

Tacking the norm of the previous relation leads to

$$\begin{aligned} |\mathrm{dev}(\boldsymbol{\tau})| &= K_e |\mathrm{dev}(\dot{\boldsymbol{\gamma}}_p)|^n + \mu\,\mathrm{tr}(\boldsymbol{\tau})/3 \\ \iff \quad |\mathrm{dev}(\dot{\boldsymbol{\gamma}}_p)| &= K_e^{-1/n} \left(|\mathrm{dev}(\boldsymbol{\tau})| - \mu\,\mathrm{tr}(\boldsymbol{\tau})/3\right)^{1/n} \end{aligned}$$

We recognize a Herschel-Bulkley [HB26] like relation, where the yield stress is proportional to the particle pressure. Note that, when $|\mathrm{dev}(\boldsymbol{\tau})| \leqslant \mu\,\mathrm{tr}(\boldsymbol{\tau})/3$, we have $\mathrm{dev}(\dot{\boldsymbol{\gamma}}_p) = 0$. Injecting this result in the previous relation, we get:

$$\mathrm{dev}(\dot{\boldsymbol{\gamma}}_p) \;=\; K_e^{-1/n} \max\left(0,\; |\mathrm{dev}(\boldsymbol{\tau})| - \mu\,\mathrm{tr}(\boldsymbol{\tau})/3\right)^{1/n} \frac{\mathrm{dev}(\boldsymbol{\tau})}{|\mathrm{dev}(\boldsymbol{\tau})|}$$

We assume a similar relation for the trace parts $\mathrm{tr}(\dot{\boldsymbol{\gamma}}_p)$ and the particle pressure $p_p = \mathrm{tr}(\boldsymbol{\tau})/3$ and then we obtain the following constitutive equation for the suspension:

$$\dot{\boldsymbol{\gamma}}_p \;=\; K_e^{-1/n} \max\left(0,\; |\mathrm{dev}(\boldsymbol{\tau})| - \mu\,\mathrm{tr}(\boldsymbol{\tau})/3\right)^{1/n} \frac{\boldsymbol{\tau}}{|\mathrm{dev}(\boldsymbol{\tau})|}$$

Next, we assume a linear relation between the deformation $\boldsymbol{\gamma}_e$ of the particle clusters deformation and the particle stress by introducing a time scale λ:

$$\boldsymbol{\tau} \;=\; \frac{(1-d)K_e}{\lambda^n}\boldsymbol{\gamma}_e \tag{2}$$

where $d \in [0,1]$ is a damage variable that represents the density of contacts loss between particles and $G = K_e/\lambda^n$ is the elastic modulus of the undamaged particle cluster, e.g. when $d = 0$. Otherwise, when $0 < d < 1$, some contacts are loss and the effective elastic modulus of the damaged particle clusters is $(1-d)G$. See e.g. [Mau92, p. 206] for an introduction to damage. From (1) we get also $\dot{\boldsymbol{\gamma}}_p = \dot{\boldsymbol{\gamma}} - \dot{\boldsymbol{\gamma}}_e$. Replacing in the previous relation, we get

$$\dot{\boldsymbol{\gamma}}_e + \frac{(1-d)^{\frac{1}{n}}}{\lambda} \max\left(0,\; |\mathrm{dev}(\boldsymbol{\gamma}_e)| - \mu\,\mathrm{tr}(\boldsymbol{\gamma}_e)/3\right)^{1/n} \frac{\boldsymbol{\gamma}_e}{|\mathrm{dev}(\boldsymbol{\gamma}_e)|} \;=\; \dot{\boldsymbol{\gamma}}$$

The characteristic time λ is associated to the particle clusters that come back to an equilibrium state after deformation, and this time scale is due to lubrication in thin spaces between particles (see e.g. [Lar99, p. 270]). The rate of deformation tensor $\dot{\boldsymbol{\gamma}}$ is identified to the symmetric part of the gradient of velocity $D(\boldsymbol{u})$, where $\boldsymbol{u}$ is the velocity of the suspension. Also, the time derivative $\dot{\boldsymbol{\gamma}}_e$ is represented by the upper convected tensor derivative, denoted by $\mathscr{D}\boldsymbol{\gamma}_e/\mathscr{D}t$ (see [Sar16], chap 4).

$$\frac{\mathscr{D}\boldsymbol{\gamma}_e}{\mathscr{D}t} + \frac{(1-d)^{\frac{1}{n}}}{\lambda} \max\left(0, \frac{|\mathrm{dev}(\boldsymbol{\gamma}_e)| - \mu\,\mathrm{tr}(\boldsymbol{\gamma}_e)/3}{|\mathrm{dev}(\boldsymbol{\gamma}_e)|^n}\right)^{\frac{1}{n}} \boldsymbol{\gamma}_e \;=\; 2D(\boldsymbol{u})$$

This is an elastoviscoplastic constitutive equation: see e.g. [Sar07, Sar09] for similar models. The total Cauchy stress tensor writes:

$$\boldsymbol{\sigma}_{\mathrm{tot}} \;=\; -p\boldsymbol{I} + 2\eta(|2D(\boldsymbol{u})|)\, D(\boldsymbol{u}) + \frac{(1-d)K_e}{\lambda^n}\boldsymbol{\gamma}_e \tag{3}$$

Finally, the base suspension viscosity $\eta(\dot{\gamma})$ is given by a power law function

$$\eta(\dot{\gamma}) \;=\; K_p |\dot{\gamma}|^{m_p - 1} \tag{4}$$

where K_p and m_p are material parameters.

2.2 Problem statement

The problem can be closed as a system of four equations and four unknowns $\boldsymbol{\gamma}_e$, the particle clusters deformation, d, the contact damage, $\boldsymbol{u}$, the velocity, and p, a Lagrange multiplier associated to the incompressibility constraint of the mixture that interprets as the pressure in the fluid phase:

$$\frac{\mathscr{D}\boldsymbol{\gamma}_e}{\mathscr{D}t} + \frac{(1-d)^{\frac{1}{n}}}{\lambda} \max\left(0, \frac{|\mathrm{dev}(\boldsymbol{\gamma}_e)| - \mu\,\mathrm{tr}(\boldsymbol{\gamma}_e)/3}{|\mathrm{dev}(\boldsymbol{\gamma}_e)|^n}\right)^{\frac{1}{n}} \boldsymbol{\gamma}_e - 2D(\boldsymbol{u}) = 0 \tag{5a}$$

$$\lambda_d \frac{Dd}{Dt} + d - \mathrm{dam}(\boldsymbol{\gamma}_e, D(\boldsymbol{u})) = 0 \tag{5b}$$

$$\rho\frac{D\boldsymbol{u}}{Dt} + \mathbf{div}\left(-p\boldsymbol{I} + 2\eta(|2D(\boldsymbol{u})|)\,D(\boldsymbol{u}) + \frac{(1-d)K_e}{\lambda^n}\boldsymbol{\gamma}_e\right) = \rho\boldsymbol{g} \tag{5c}$$

$$\mathrm{div}\,\boldsymbol{u} = 0 \tag{5d}$$

The problem is closed by suitable initial and boundary conditions. The elastoviscoplastic constitutive equation (5a) is coupled with an equation for the damage evolution (5b) and with the conservation of momentum (5c) and mass of the mixture (5d). In (5c), $D/Dt = \partial/\partial t + \boldsymbol{u}.\nabla$ denotes the Lagrange derivative and ρ is the density of the mixture. Note that the volume fraction ϕ is supposed to be constant during the flow: the time scale for migration is large and the possible variation of the volume fraction is here supposed negligible. Otherwise, the system could be also couped by an additional diffusion equation for the volume fraction (see e.g. [MM06]).

The $\mathrm{dam}(\boldsymbol{\gamma}_e, D(\boldsymbol{u}))$ term in (5b) denotes a damage function that takes its values in $[0, 1]$. It locally depends upon the flow direction and the particle clusters. The time scale λ_d is associated to contacts that establishes or are loss. The detailed expression for the damage function will be discussed in details in the next section 2.1 devoted to time-dependent flow.

3 Time dependent shear flows

3.1 The damage function

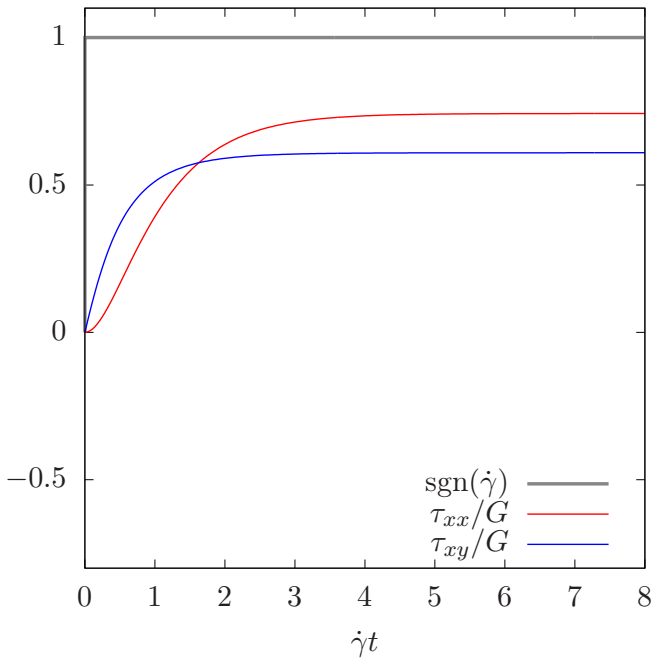

Figure 2: Shear startup from rest ; Computations are performed with a characteristic time $\lambda = 0.35$.

For a stationary flow, the deformation rate compresses the particle clusters and contacts are maintained: in that case, the damage variable d, that represents loss of contacts, is zero.

When an imposed shear rate changes from $\dot{\gamma} \neq 0$ to zero, experimental observations (see [KPGM02], Fig. 3) showed that both the the particle pressure $p_p = \tau_{xx}/3$ and the shear stress σ_{xy} fall very fast to zero. In that case, the deformation rate does no more compresses the particle clusters and contacts are loss: it means $d = 1$. It could be effective on a very short time scale by some small repulsion forces between particles: particles stay very close but without contacts. The associated time scale is very small i.e. $\lambda_d \approx 0$ in (5b). From (2) and as $d = 1$ we obtain $\boldsymbol{\tau} = 0$. Next, as the deformation rate is zero, we get from (3) that $\sigma_{xy} = 0$. Observe that (3) reduces to the time derivative of the structure tensor equal to zero: the structure tensor $\boldsymbol{\gamma}_e$ of the particle clusters remains unchanged while contacts are loss ($d = 1$).

Next, there is two possibilities:

- If the shear restarts suddenly in the same direction, experimental observations (see [KPGM02], Fig. 3) showed that both the the particle $p_p = \tau_{xx}/3$ and the shear stress σ_{xy} jump very fast to the previous stationary value. Suddenly, contacts are restored between particles in the suspension: d changes from 1 to 0. As the structure tensor $\boldsymbol{\gamma}_e$ was unchanged and now $d = 0$, from (2), the previous stationary value of $\boldsymbol{\tau}$ is restored on a with short time scale.

- Otherwise, if we suddenly change the shear rate zero to the opposite of its previous value $-\dot{\gamma}$, i.e. a shear reversal, from [NSH+02], Fig. 3, we observe that the particle pressure p_p increases progressively from zero to its previous stationary value while the shear stress σ_{xy} progressively decreases from zero to the opposite of its previous stationary value. When the deformation rate is reversed, then $d = 1$, i.e. contacts are restored. Next, from (5a), the tensor $\boldsymbol{\gamma}_e$ evolves from its previous conserved value $\boldsymbol{\gamma}_e$ to a new stationary one, as the right-hand-side of (5a) has been changed from $D(\boldsymbol{u})$ to $-D(\boldsymbol{u})$

(See Fig. 3). An detailed investigation shows that the new stationary solution has the same normal component $\gamma_{e,xx}$ while $\gamma_{e,xy}$ has opposite sign. Thus, the particle pressure converges to the same stationary value while tends to change of sign σ_{xy}.

All these deductions from the system of equations are conform to experimental observation. For the damage function, we choose:

$$\mathrm{dam}(\boldsymbol{\gamma}_e, D(\boldsymbol{u})) \;=\; \begin{cases} 1 & \text{when } |D(\boldsymbol{u})| \leqslant \dot{\gamma}_c \\ 0 & \text{when } |D(\boldsymbol{u})| > \dot{\gamma}_c \text{ and } \boldsymbol{\gamma}_e : D(\boldsymbol{u}) \geqslant -\dot{\gamma}_c \\ \dfrac{|\boldsymbol{\gamma}_e : D(\boldsymbol{u})|}{|\mathrm{dev}(\boldsymbol{\gamma}_e)|\,|D(\boldsymbol{u})|} & \text{otherwise} \end{cases} \tag{6}$$

It means that when the deformation rate $D(\boldsymbol{u})$ acts in compression on the particle clusters, then contacts are reinforced and there is no damage. Otherwise, the deformation rate acts in dilatation, tends to separate the particles, contacts are loss and the particle clusters are damaged. Here, $\dot{\gamma}_c \geqslant 0$ denotes a critical shear rate: its action balances the repulsion forces between particles, represented by a repulsion critical stress $\sigma_r = \eta(\phi, \dot{\gamma}_c)\dot{\gamma}_c$. In practice, $\dot{\gamma}_c$ is very small and is used to avoid a division by a too small number.

The solution is represented on Fig. 2 for a startup of shear at $t = 0$ with a shear rate $\dot{\gamma} > 0$ where $\boldsymbol{\gamma}_e(t{=}0) = 0$. The material is undamaged and $\boldsymbol{\tau}_e = \dfrac{K_e}{\lambda^n}\boldsymbol{\gamma}_e$ growth and tends to a stationary value. Fig. 3 represents a more complex situation: the material is first sheared with a negative shear $-\dot{\gamma}$ and then, after a period of rest, the shear rate is reversed to $\dot{\gamma} > 0$ at $t = 0$. During the period of rest, the material is damaged and $\boldsymbol{\gamma}_e = 0$ while $\boldsymbol{\gamma}_e$ is constant. It means that the particle clusters are unchanged during the period of rest. At $t = 0$, the shear starts in the positive direction: the the particle clusters rotates slowly to the opposite angle, from about $-\pi/6$ to $\pi/6$. During the rotation, the damage progressively decreases and reaches zero when the inclination angle is also zero. The particle stress $\boldsymbol{\tau}$ develops from zero to a stationary value. Dotted lines represents $\boldsymbol{\gamma}_e$ values. Observe that the time scale to reach the new stationary solution is of about $2\dot{\gamma}^{-1}$, as observed in experiments (see e.g. [KPGM02], Fig. 5).

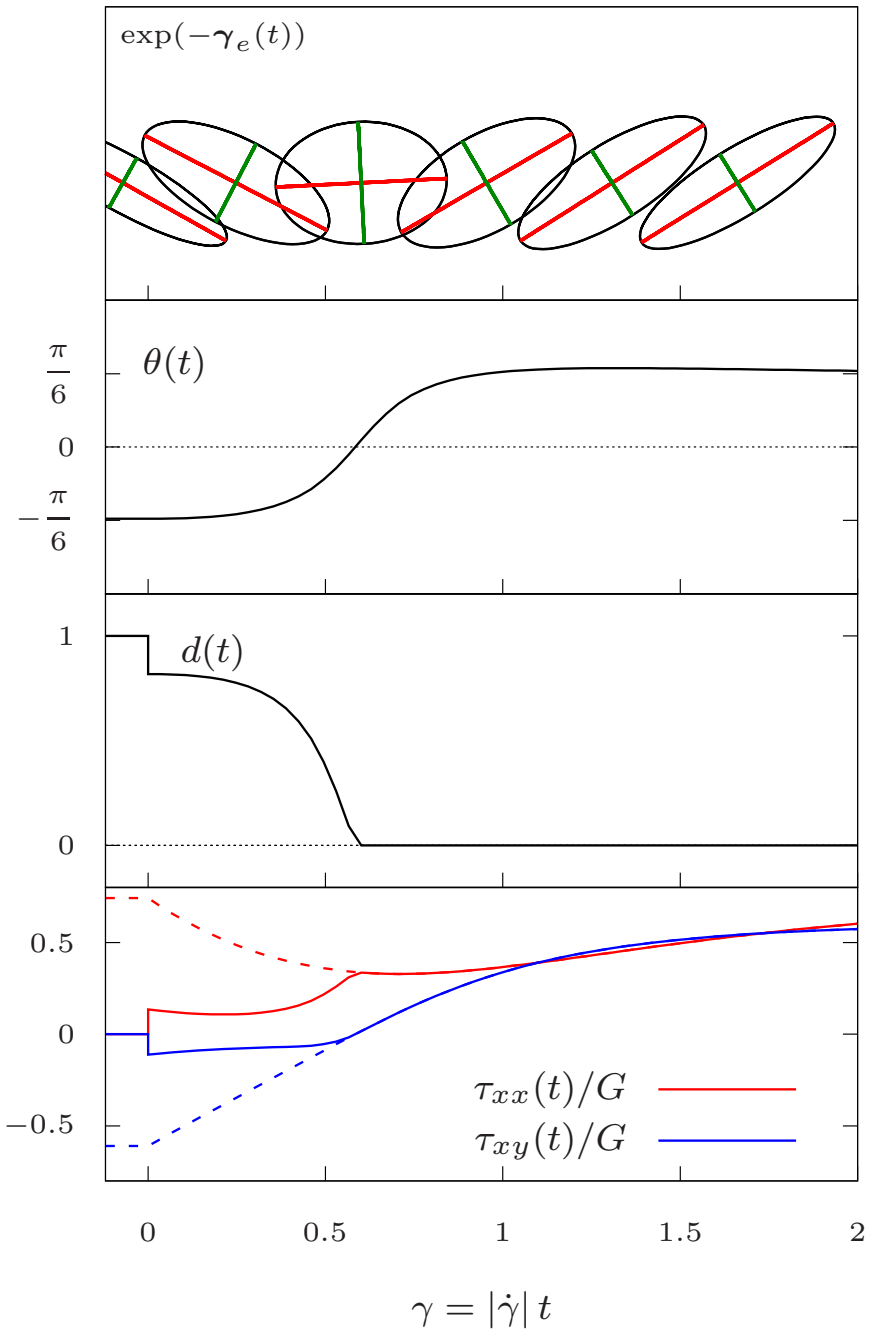

Figure 3: Shear reversal at $t = 0$: representation of the texture tensor $\exp(-\boldsymbol{\gamma}_e(t))$ versus time as an ellipse: eigenvector associated to compression (resp. dilatation), i.e. to the positive (resp. negative) eigenvalue of $\boldsymbol{\gamma}_e$ is represented in red (resp. green). On the bottom, plots for the sign of the shear stress $\dot{\gamma}$, the inclination angle $\theta(t)$ of the ellipse, the damage $d(t)$ and the particle stress $\boldsymbol{\tau}$ with $\boldsymbol{\gamma}_e$ in dotted lines. Computations are performed with a characteristic time $\lambda = 0.35$.

3.2 Comparison with experiments

We aim at comparing our model for unsteady shear flows with experimental measurements. In 2001, Blanc [Bla11, sec 3.3] (see also [BPL11a, BPL11b, BLMP13]) performed shear reversal experiments in a Couette geometry. The author consider a suspension of polymethyl methacrylate (PMMA) spherical particles in a Newtonian oil. The experiments have been performed with an imposed torque and, for each volume fraction, it is adjusted in order to obtain similar angular velocities. Neglecting the variations between the gap, the shear rate is here assumed as constant and the model is solved here as a simple shear flow. All geometrical and material parameters of the experiment are grouped in table 1. The volume

description	unit	symbol	value
fluid viscosity	$Pa.s$	η_0	1.03
power law index		m_p	0.9
outer radius	m	R_e	$2.4\,10^{-2}$
inner radius	m	R_i	$1.4\,10^{-2}$
radius for measures	m	R_c	$0.77 \times R_e$
height	m	L	$4.5\,10^{-2}$
torque	$N.m$	T_m	*imposed*
angular velocity	s^{-1}	ω	*measured*
shear stress	Pa	$\sigma_{r\theta}$	$\dfrac{0.818 \times T_m}{2\pi L R_c^2}$
shear rate	s^{-1}	$\dot{\gamma}$	$\dfrac{\omega R_i}{R_e - R_i}$

Table 1: Shear reversal: experimental parameters, from [Bla11, sec 3.3].

fraction ϕ is varying in the range $[0.3, 0.5]$. In this volume fraction range, the suspension has been founded slightly shear-thinning: the viscosity can be expressed with the power-law (4) where the power index $m_p = 0.9$. During experiments, the torque T_m is adjusted in order for the angular velocity to reach similar values in the stationary regime.

The present model involves two material parameters with fixed values: the power-law index $n = 2/3$ and the friction coefficient $\mu = 0.7$. As shown in appendix A, the choice for n leads to a linear dependence of the normal stress difference and particle pressure versus the shear rate for stationary shear flows. The choice $\mu = 0.7$ corresponds to an usual value of the friction coefficient (see e.g. [BGP11]). The time scale of the damage parameter is chosen as very small: $\lambda_d = 10^{-4}$.

There are still three model parameters to determine: λ, K_e and K_p. For each volume fraction, these three parameters are adjusted to experimental measurements (from [Bla11], Fig. 3.17) of the apparent viscosity. In simple shear flow, the set of equations reduces to a time-dependent system of ordinary differential equation that are solved by the `lsode` library [RH93], as interfaced in the `octave` software [EBH11]. Fig. 4 presents a comparison between the model prediction and the experimental measurements of the apparent viscosity for the shear reversal. Observe that, for the first time, the sudden decrease of the apparent viscosity and its relaxation to the stationary value are qualitatively and quantitatively well represented by a continuous model. Indeed, there are three regimes: first, we observe an instantaneous decrease, then, a minimum is reached with a smooth shape, and finally, the apparent viscosity increases regularly until it reaches its stationary value. The only discrepancy between the model prediction and experimental measurements concerns the first regime, at the vicinity the minimum, where the model predicts a slow increases. Observe that the apparent viscosity, as measured during experiments, increases slowly for large deformations γ: a possible cause could be the slow migration of particles in the Couette gap, due to a small variation of the shear rate between the gap. The table at the bottom of Fig. 4 groups, for each

volume fraction, the values used for the three model parameters λ, K_e and K_p.

Fig. 5 presents the dependency upon the volume fraction ϕ of the three adjusted model parameters λ, K_e and K_p. Observe the regularity of these dependencies: this suggests a best fit procedure based on the following material functions:

$$\lambda(\phi) = \lambda_0 \exp(-\alpha\phi) \tag{7a}$$

$$K_e(\phi) = \bar{K}_e \left(1 - \frac{\phi}{\phi_m}\right)^{-\beta_2} \tag{7b}$$

$$K_p(\phi) = \bar{K}_p \left(1 - \theta_p + \left(\frac{5}{2} - \frac{\beta\theta_p}{\phi_m}\right)\phi + \theta_p \left(1 - \frac{\phi}{\phi_m}\right)^{-\beta}\right) \tag{7c}$$

Indeed, the values of λ vs ϕ are aligned on the semi-logarithmic plot Fig. 5.top-left: this suggests an exponential dependency (7a). Conversely, the values of K_e vs ϕ are aligned on on the log-log plot Fig. 5.top-right: this suggests a power-law dependency (7b). The expression (7c) for $K_p(\phi)$ is an original extension of the Krieger-Dougherty [KD59] rule: when the volume fraction is small, its first order development coincides with the Einstein [Ein06] rule $K_p(\phi)/\bar{K}_p = 1 + 5\phi/2$ for any value of the three material parameters ϕ_m, $\beta \geqslant 0$ and $\theta_p \in [0, 1]$. The parameter ϕ_m is the maximal volume fraction of the suspension, $\beta \approx 2$ is the power-law index of the Krieger-Dougherty rule and θ_p is a balance parameter. The table on the bottom of Fig. 5 groups the values as adjusted for the parameters involved by these expressions. The best fit uses a nonlinear least square method, as implemented in [WK10].

Fig. 6 presents a sensitivity analysis of the present model upon the seven parameters λ, K_e, K_p, μ, n, m_p and λ_d around the solution obtained for $\phi = 0.47$. The effects of the three adjusted parameters λ, K_e and K_p can be interpreted as follow: λ drives the amplitude of the stationary apparent viscosity, K_e drives the slope of the transient regime and K_p the value of the minimum. Observe that the variation upon the power law indexes n and m_p have significant effects what justifies to choose them with care, whereas the variation upon the friction coefficient μ leads to small variations of the stationary apparent viscosity. Finally the damage time scale λ_d should be chosen small enough for the solution to be unchanged.

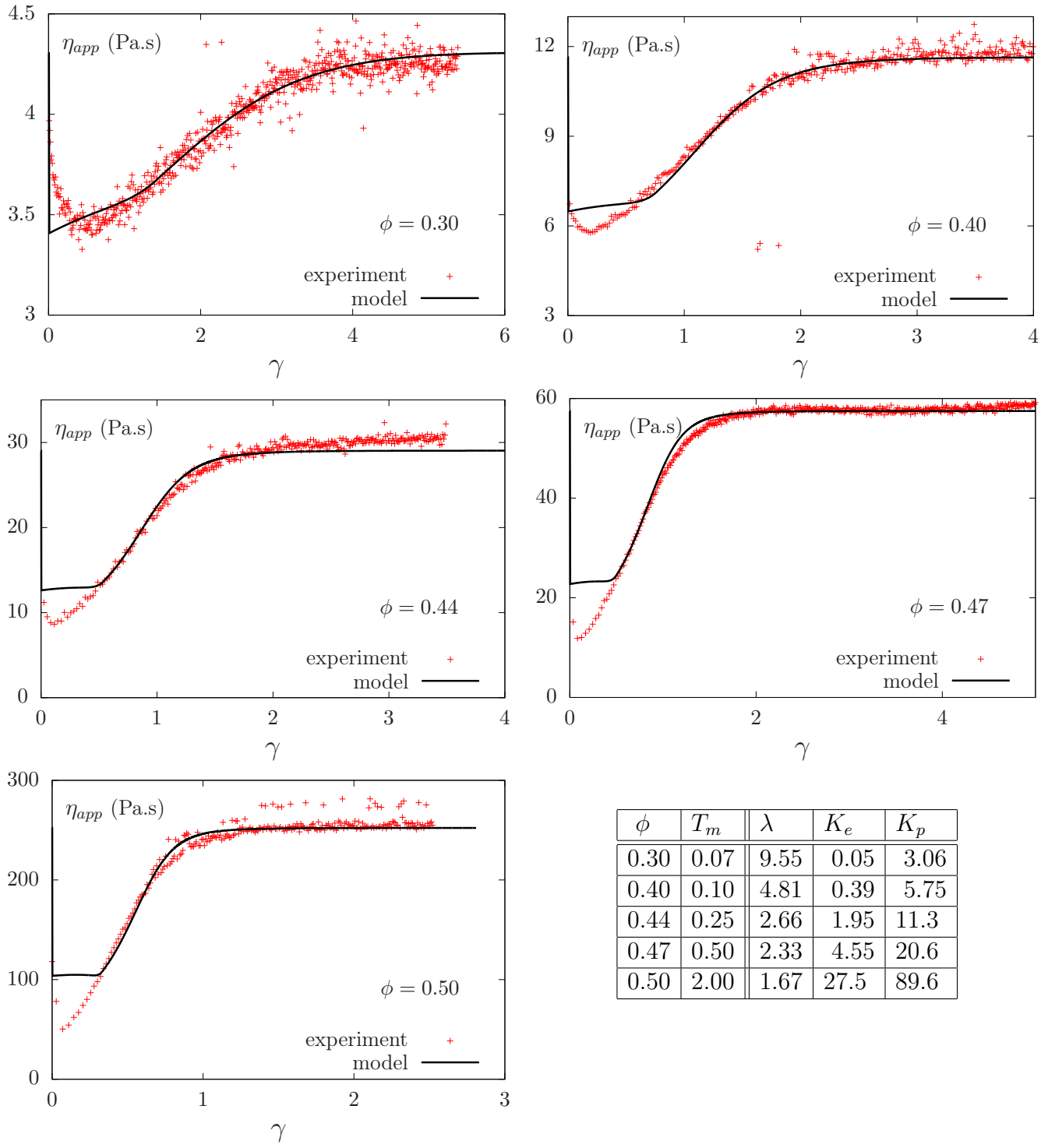

ϕ	T_m	λ	K_e	K_p
0.30	0.07	9.55	0.05	3.06
0.40	0.10	4.81	0.39	5.75
0.44	0.25	2.66	1.95	11.3
0.47	0.50	2.33	4.55	20.6
0.50	2.00	1.67	27.5	89.6

Figure 4: Shear reversal: apparent viscosity η_{app} vs deformation γ. Comparison between experimental measurements (from [Bla11], Fig. 3.17) for a PPMA suspension in a Couette geometry and computations with the present model. For each experimental conditions ϕ and T_m, the three model parameters λ, K_e, K_p are chosen from a best fit procedure. Values are grouped in the table on bottom-right.

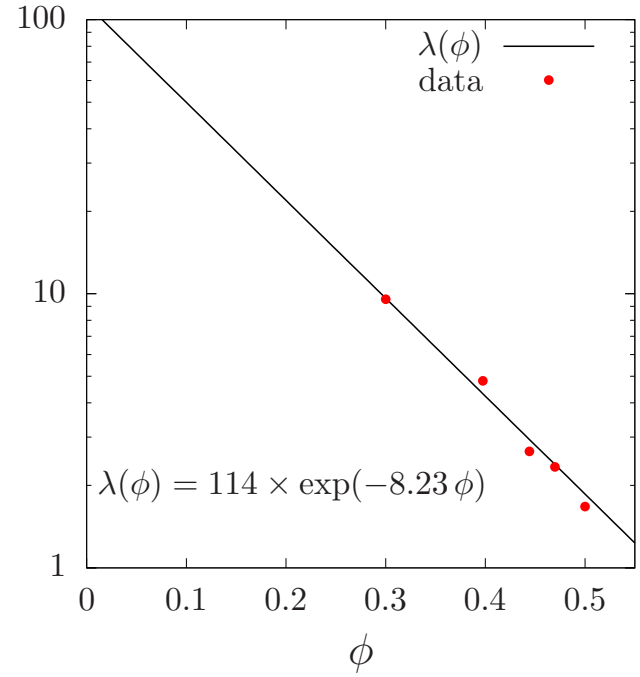

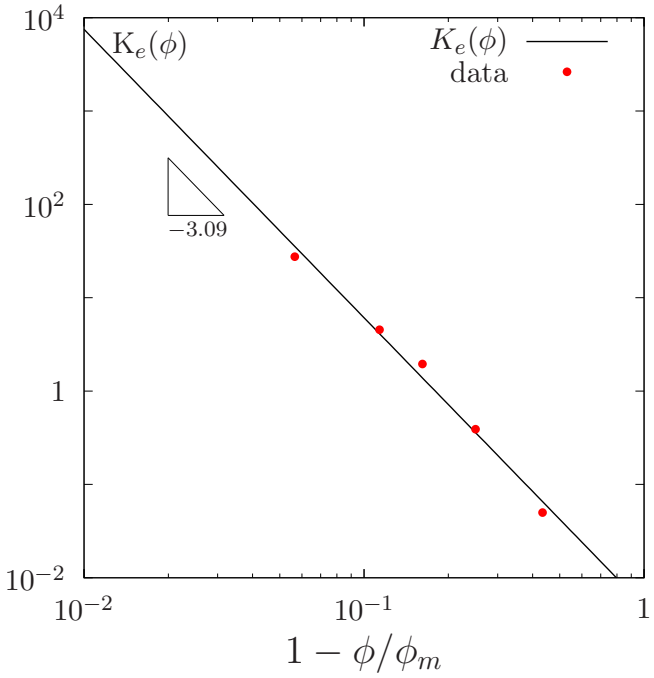

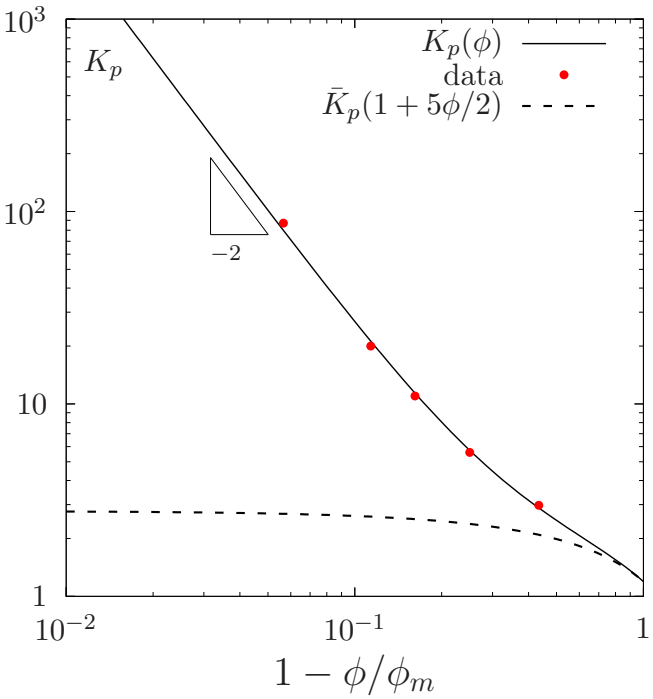

λ_0	α	$\bar{K}_e$	β_2	$\bar{K}_p$	θ_p	β	ϕ_m
1.14×10^2	8.29	4.96×10^3	3.09	1.19	0.209	2.00	0.53

Figure 5: Shear reversal: best fit versus ϕ for the three material parameters λ, K_e, K_p of the model.

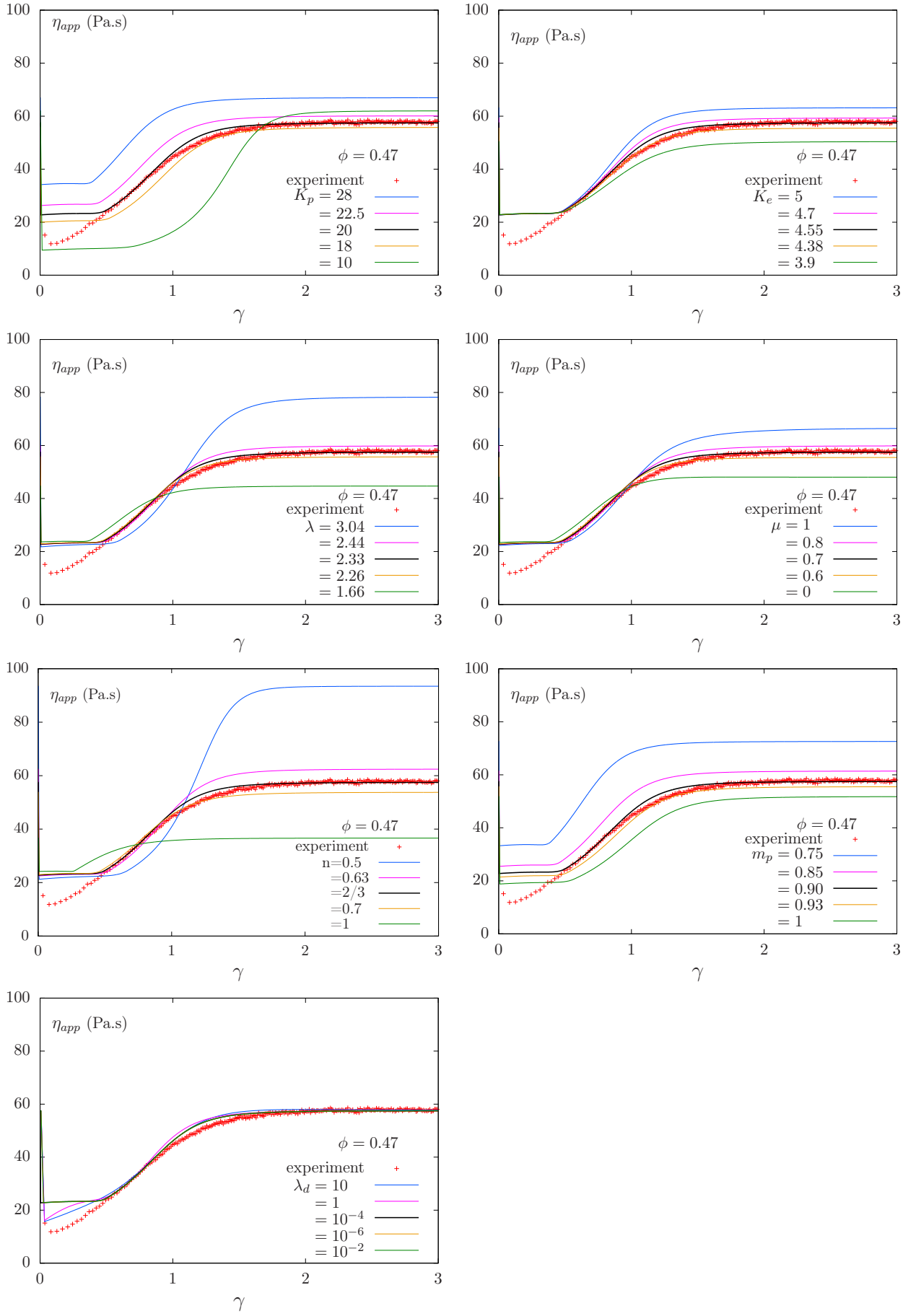

Figure 6: Shear reversal: sensitivity analysis on material parameters of the model ($\phi = 0.47$).

4 Stationary shear flow

4.1 Imposing both volume fraction and shear rate

In [ZHLJ00], Figs. 7.b and 10.b, the authors considered as Newtonian fluid a corn syrup: its viscosity $\eta_0 = 2.2$ Pa.s at 24^0C (see Fig. 6 of the paper). The rigid spheres have diameter equal to 43 μm and are suspended in the corn syrup, and the suspension is considered as non-Brownian. The geometry is a parallel plate rheometer.

The solution of the present model for a stationary simple shear flow admits an explicit expression, developed in appendix A.2. The normal stress difference $N_1 - N_2 = \tau_{xx}$ is explicitly given by (12a). As in the present section, we choose the power-law index $n = 2/3$ and the friction coefficient $\mu = 0.7$. The flow is stationary and the shear rate compresses the particle clusters, so we assume here that there is no damage of the particle clusters, i.e. $d = 0$. Thus, the damage time scale λ_d is not involved. Also, the time scale λ is undetermined, as it appears only as the ratio $G = K_e/\lambda^n$ in the expression (12a) of the stationary solution: thus, the time scale λ can be chosen as an arbitrarily constant. Note that expression (12a) for the normal stress still involves the material parameter K_e. Instead of identifying K_e from the experimental data for each value of the volume fraction ϕ, we base on the template expression (7b) and identify its two scalar parameters $\bar{K}_e$ and β_2 for the *whole* bidimensional in $(\phi, \dot{\gamma})$ experimental data set. This bidimensional identification in $(\phi, \dot{\gamma})$ bases on a nonlinear least square method, as implemented in [WK10]. The maximal volume fraction was chosen as $\phi_m = 0.67$. Fig. 7.top-left compares the normal stress difference $N_1 - N_2$, as predicted by the present model, with the experimental measurement, as given in [ZHLJ00], Fig. 10.b. Observe the good agreement between the experimental measurements and the model prediction. The model predicts, as expected, an linear dependence of the normal stress difference versus the shear rate.

Fig. 7.center-left compares the apparent viscosity $\eta_{\text{app}} = \sigma_{xy}/\dot{\gamma}$ by as predicted by the present model, with the experimental measurement, as given in [ZHLJ00], Fig. 7.b. Observe also the good agreement between the model prediction and the measures. The exact solution of the model is given in (12c), replacing the base viscosity $\eta(\dot{\gamma})$ by its expression (4). The base viscosity $\eta(\dot{\gamma})$ involves two material parameters K_p and m_p. As for the normal stress difference, we choose to identify globally, for the whole experimental data set, these material parameters: we base on the template expression (7c) for K_p. The corn-syrup suspension was founded shear-thinning with a power-law index m_p that varies with the volume fraction and we use:

$$m_p(\phi) \quad = \quad 1 - \frac{\exp(\nu_p \phi) - 1}{\exp(\nu_p \phi_m) - 1} \tag{8}$$

Thus, there four four material parameters: $\bar{K}_p$, β, θ_p, ν_p We use $\beta = 2$ while the three others parameters are adjusted on the whole bidimensional experimental data set.

The right column on Fig. 7 plots the material functions $K_e(\phi)$, $K_p(\phi)$ and $\lambda(\phi)$ while the table on the bottom of Fig. 7.bottom groups the numerical values of the associated scalar parameters. It is remarkable that the model is able to predict such a complex behavior with very few adjustable scalar parameters.

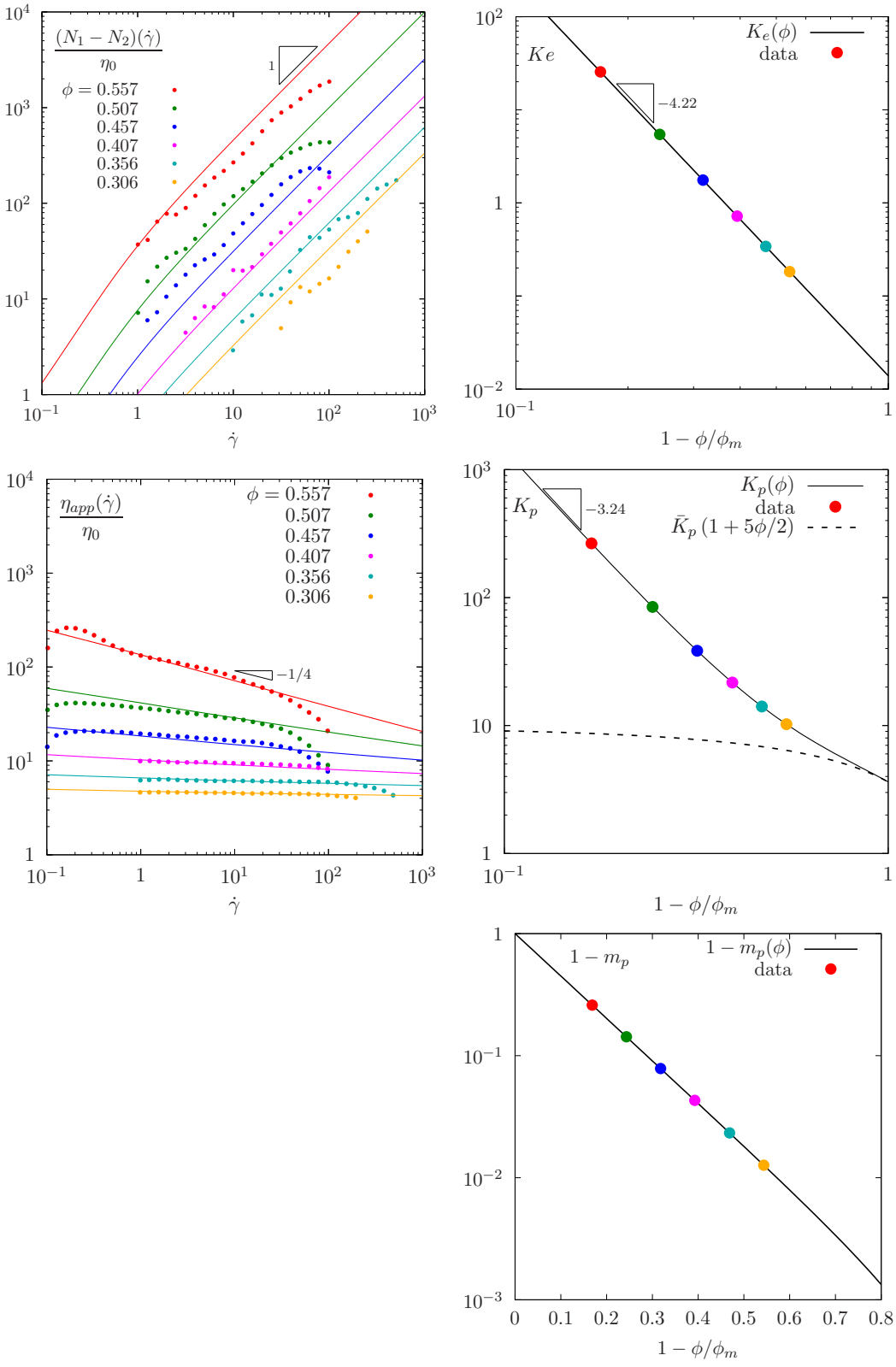

λ_0	α	$\bar K_e$	β_2	ϕ_m	$\bar K_p$	β	θ_p	ν_p
1	0	1.39×10^{-2}	4.22	0.67	3.62	3.24	0.22	11.9

Figure 7: Stationary shear. Comparison of normal stress (top-left) and shear stress (bottom-left) as predicted with the present model and as measured with a suspension in a corn syrup, from [ZHLJ00], Fig. 7.b and 10.b.

4.2 Imposing both particle pressure and shear stress

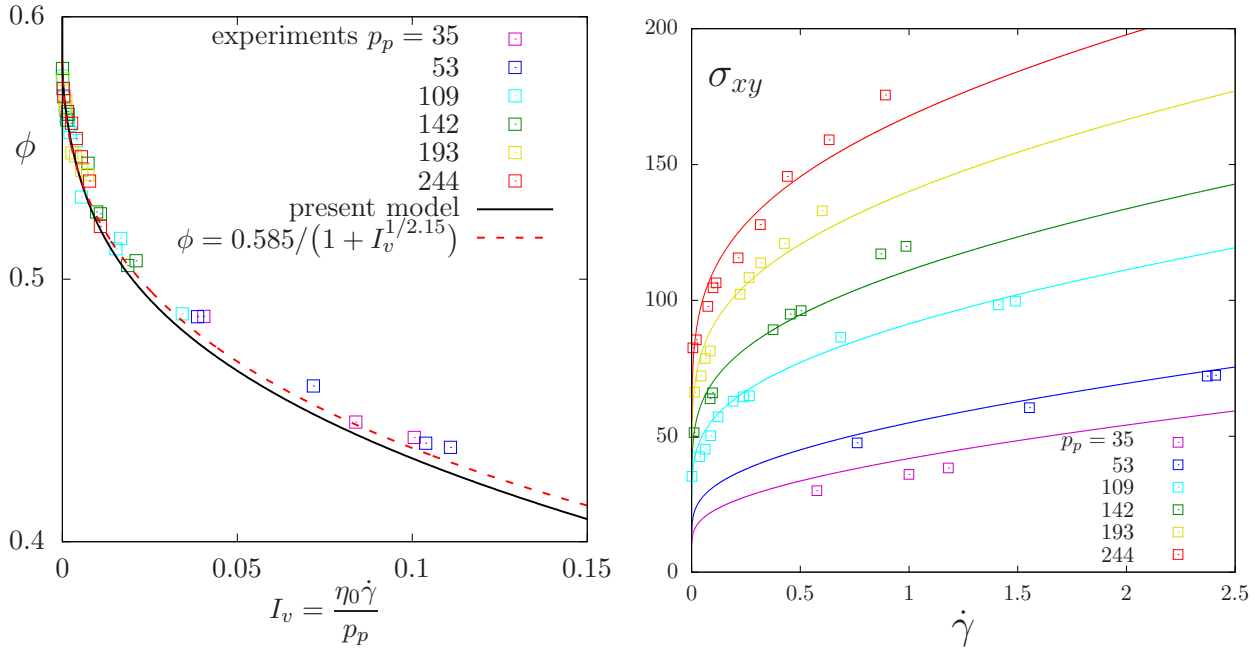

λ_0	α	$\bar{K}_e$	β_2	ϕ_m	$\bar{K}_p$	β	θ_p	ν_p
1	0	0.447	2.97	0.585	3.43	1.89	0.807	0

Figure 8: Stationary shear. Comparison of the present model prediction with experimental measures: (left) ϕ vs $I_v = \eta_0 \dot{\gamma}/p_p$, from [BGP11], Fig. 2.c ; (right) σ_{xy} vs $\dot{\gamma}$ from [BGP11], Fig. 2.a(insert).

In 2011, Boyer et al. [BGP11] performed experimental measurements of both shear rate $\dot{\gamma}$ and volume fraction ϕ, while the particle pressure p_p and the shear stress σ_{xy} are imposed. The spherical particles are suspended in a triton x-100/water/zinc chloride mixture of viscosity $\eta_0 = 3.1$ P.s.

Fig. 8.top-left presents the volume fraction versus the dimensionless quantity $I_v = \eta_0 \dot{\gamma}/p_p$, as predicted by the model together with experimental measurements from [BGP11], Fig. 2.c. Observe the excellent agreement between the model prediction and the experimental data. The empirical approximation

$$\phi \quad = \quad \phi_m \left(1 + I_v^{1/\hat{\alpha}}\right)^{-1} \tag{9}$$

suggested in [BGP11], relation (7), with $\hat{\alpha} = 2$ has been here slightly improved with $\hat{\alpha} = 2.15$: it is also represented by a dotted red line. The choice of the material parameters of the model has been performed using a methodology similar to those of the previous paragraph. The power-law index is $n = 2/3$ and the friction coefficient is $\mu = 0.7$. The flow is stationary and the shear rate compresses the particle clusters, so we assume here that there is no damage of the particle clusters, i.e. $d = 0$. Thus, the damage time scale λ_d is not involved. Also, the time scale λ is undetermined: thus, it can be chosen as an arbitrarily constant. In appendix A.3, relation (15) provides an explicit relation of I_v versus ϕ from the solution of the model. It remains to determine the material parameter K_e. Based on (7a) for the dependence of K_e upon ϕ, the two associated scalar parameters $\bar{K}_e$ and β_2 are identified globally on the bidimensional (ϕ, p_p) experimental data set from [BGP11], Fig. 2.c.

Fig. 8.top-right presents the shear stress σ_{xy} versus the shear rate $\dot{\gamma}$ as predicted by the model together with experimental measurements from [BGP11], Fig. 2.a(insert). Observe the good agreement between the model and the experimental data. Experimental data from [BGP11], Fig. 2.a(insert) has been used to identify additional model parameters associated to the base viscosity $\eta(\dot{\gamma})$ of the mixture, as expressed by

the power law (4). It involves two material parameters K_p and m_p. The shear-thinning was founded to be negligible for the present fluid, and we choose $m_p = 1$. Relation (7c) is considered for the dependence of K_p upon the volume fraction ϕ. Relation (16) in appendix A.3 explicitly solves the present model and furnishes an expression of σ_{xy} that depends only on $\dot\gamma$ and p_p. The remaining scalar parameters $\bar K_p$, β and θ_p are identified using the bidimensional (ϕ, p_p) data set available from experimental measurements of $\dot\gamma$ and ϕ from [BGP11], Fig. 2.a(insert). The table on the bottom of Fig. 8 summarizes the values of the scalar parameters.

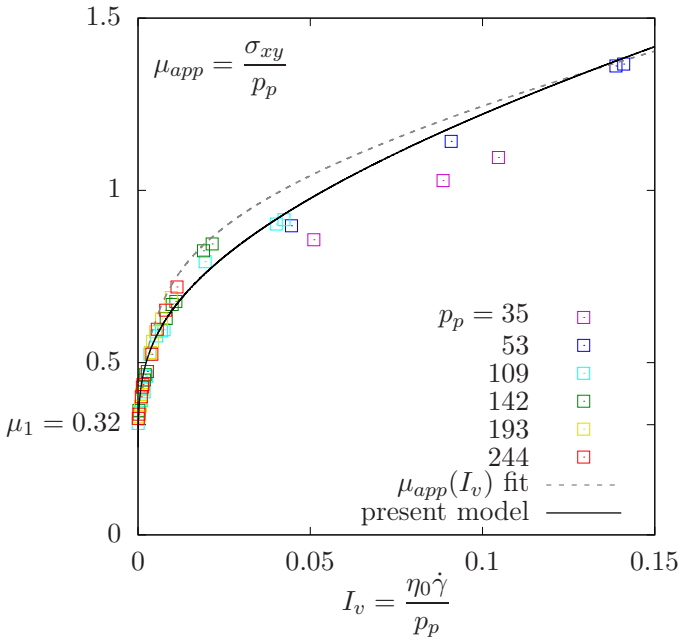

Figure 9: Stationary shear. Apparent friction coefficient $\mu_{\rm app} = \sigma_{xy}/p_p$ vs $I_v = \eta_0\dot\gamma/p_p$. Comparison of the present model prediction with experimental measures from [BGP11], Fig. 2.a.

Fig. 9 presents the dimensionless apparent friction coefficient $\mu_{\rm app} = \sigma_{xy}/p_p$ versus the dimensionless number $I_v = \eta_0\dot\gamma/p_p$. All the experimental data, and also the model predictions, seems to merge on an unique master curve: its true for small I_v but the present model predicts that these curves start to separate for large I_v. Following [BGP11], relation (6), we plot on Fig. 9 by a dotted black line the following empirical approximation:

$$\mu_{\rm app}(I_v) \quad = \quad \mu_1 + \frac{\mu_2 - \mu_1}{1 + I_0/I_v} + I_v + \frac{5\phi_m}{2}\sqrt{I_v}$$

with $\phi_m = 0.585$, $\mu_1 = 0.32$, $\mu_2 = 0.7$ and $I_0 = 0.005$. Observe that this approximation captures also well the main behavior. Recall that, in the present model, the friction coefficient is constant: this variation of the apparent friction coefficient $\mu_{\rm app} = \sigma_{xy}/p_p$ is due to the dependency of the shear stress σ_{xy} upon the normal stress τ_{xx}, via τ_{xy}, and thus, upon the particle pressure $p_p = \tau_{xx}/3$. Thus, thanks to our tensorial model that predicts normal stresses, there is no need of any dependence of the friction coefficient upon I_v, as proposed in [BGP11].

4.3 Comparison with Deboeuf et al. (2009) experiment

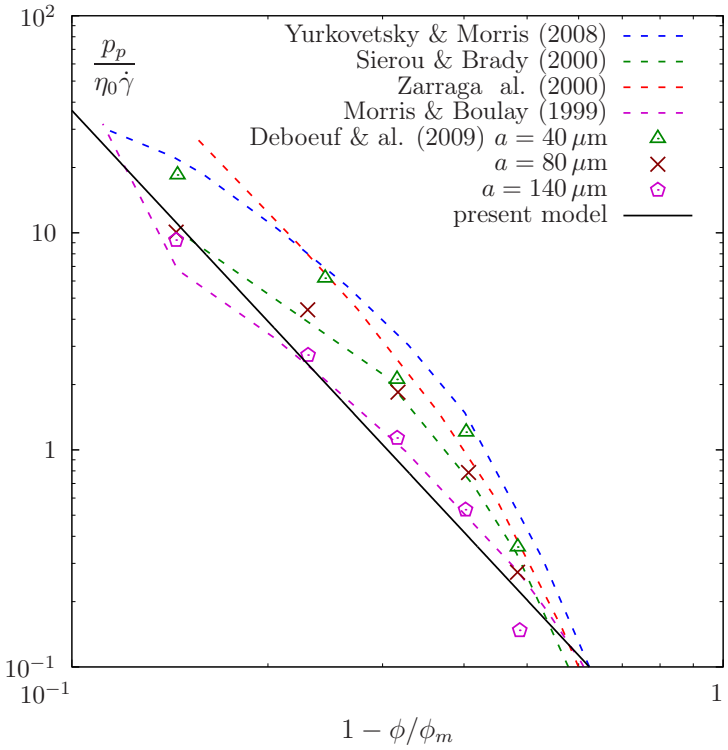

λ_0	α	$\bar K_e$	β_2	ϕ_m	$\bar K_p$	β	θ_p	ν_p
1	0	1.66×10^{-2}	3.23	0.585	–	–	–	–

Figure 10: Comparison of the present model prediction with experimental measures from [DGM+09], experimental correlations from [ZHLJ00], Stokesian simulations [YM08, SB02] and modeling [MB99].

Experimental measurements of the particle pressure p_p proposed by Deboeuf *et al.* [DGM+09] showed that its varies roughly linearly with $\dot\gamma$. This observation is confirmed by the present model: from the asymptotic analysis (13b) in appendix A, we obtain, for large $\dot\gamma$:

$$\frac{p_p}{\eta_0\dot\gamma} = \frac{2\lambda(\phi)^{1-n}K_e(\phi)}{\eta_0 c_{n,\mu}} \quad \text{for } \dot\gamma \gg 1$$

Fig. 10 plots this expression versus ϕ together with experimental measurements and others computational approaches. The suspension balance model from Morris and Boulay [MB99] corresponds to the expression $\eta_n(\phi) = p_p/(\eta_0\dot\gamma)$: it is also displayed, together with values of p_p from Stokesian simulations at Peclet number 1000 [YM08] and infinite Peclet [SB02], obtained with weak and zero thermal motion, respectively. Our model prediction is in remarkable agreement with both experimental measurements and simulation.

4.4 Depletion angle and pair distribution function

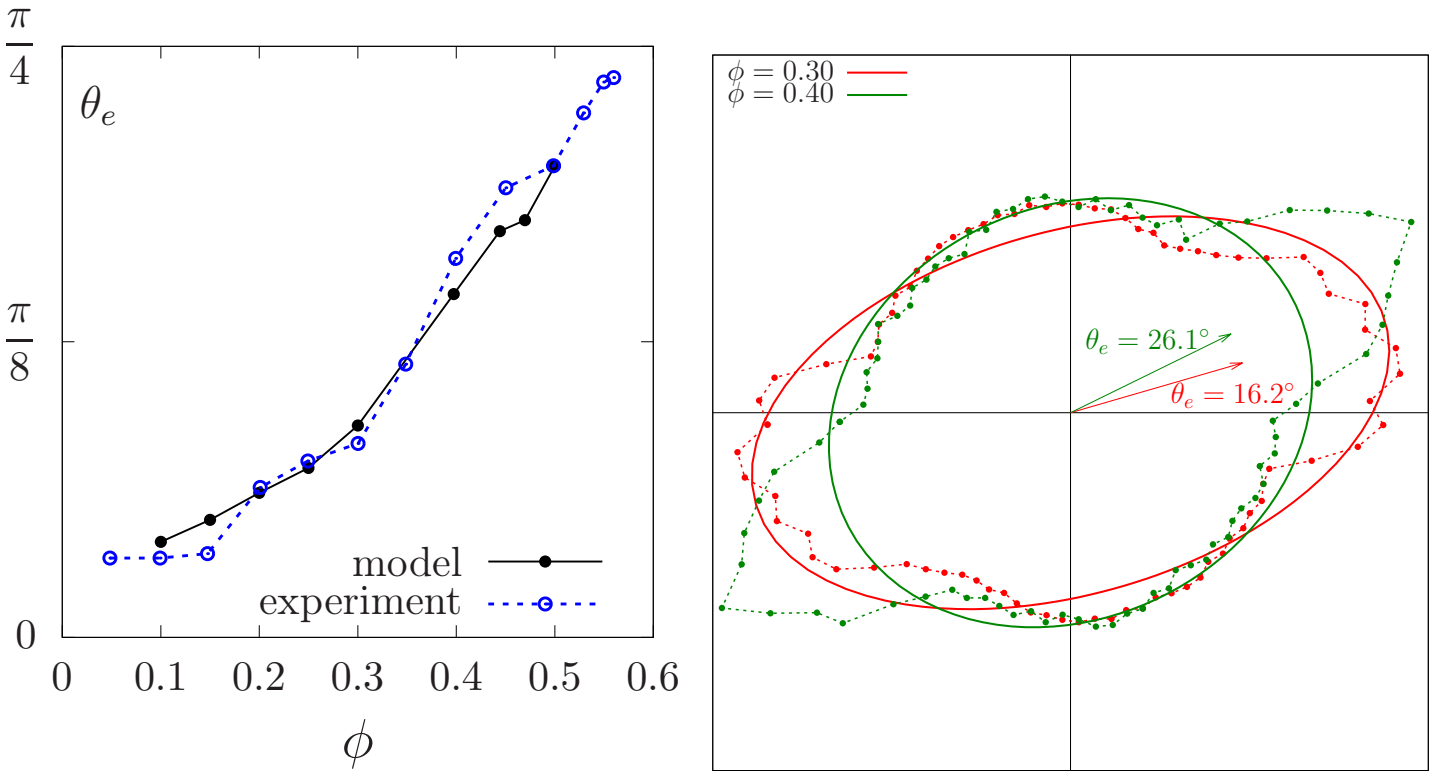

Figure 11: (left) Depletion angle θ_e versus ϕ: comparison between the model prediction (solid line) and experimental data from [Bla11], Fig. 5.11 (dotted lines). (right) Pair distribution function: comparison between the model prediction with the texture tensor $\langle \boldsymbol{\ell} \otimes \boldsymbol{\ell} \rangle = \exp(-0.2\,\boldsymbol{\gamma}_e)$ represented as an ellipse (solid lines) and the experimental data of $g(\theta)$ from [Bla11], Fig. 5.10, represented as $r = g(\theta)^{-1/2}$ versus θ in (r, θ) polar coordinates (dotted lines).

Following [BLMP13], we introduce the pair distribution function. We consider a particle p and denote by $\boldsymbol{x}_p$ the center of the particle. For any neighbor particle q of p, in the sense that there is no others particles between p and q, we denote by $\boldsymbol{\ell}$ the vector $\boldsymbol{x}_q - \boldsymbol{x}_p$. The second order tensor $\boldsymbol{\ell} \otimes \boldsymbol{\ell}$ associated with this pair distribution is symmetric. Let $\langle . \rangle$ denotes the averaging operator in a representative elementary volume (REV). Note that $\langle \boldsymbol{x}_p \rangle$ is the barycenter of the REV. Then, any point in the REV writes as $\langle \boldsymbol{x}_p \rangle + \boldsymbol{v}$ where $\boldsymbol{v} \in \mathbb{R}^3$. We assume that the distribution is invariant in the vertical direction and use the polar coordinates. Let θ be the second polar coordinate of $\boldsymbol{v}$ and θ_ℓ be the second polar coordinate of $\boldsymbol{\ell}$. Let $\mathcal{E} = \{\boldsymbol{v},\ {}^t\boldsymbol{v}\langle \boldsymbol{\ell} \otimes \boldsymbol{\ell} \rangle \boldsymbol{v} = 1\}$ be the ellipse associated to $\langle \boldsymbol{\ell} \otimes \boldsymbol{\ell} \rangle$ and represented on Fig. 1. We have:

$$\begin{aligned} \boldsymbol{v} \in \mathcal{E} &\Leftrightarrow \langle {}^t\boldsymbol{v}(\boldsymbol{\ell} \otimes \boldsymbol{\ell})\boldsymbol{v} \rangle = 1 \\ &\Leftrightarrow \left\langle (\boldsymbol{v}.\boldsymbol{\ell})^2 \right\rangle = 1 \\ &\Leftrightarrow \|\boldsymbol{v}\|^{-2} = \left\langle \|\boldsymbol{\ell}\|^2 \cos(\theta - \theta_\ell)^2 \right\rangle \end{aligned}$$

We now consider the averaging for $\|\boldsymbol{\ell}\| = 2a$ only and we get

$$\boldsymbol{v} \in \mathcal{E} \Leftrightarrow \|\boldsymbol{v}\|^{-2} = 4a^2 \left\langle \cos(\theta - \theta_\ell)^2 \right\rangle$$

We introduce $G(\theta) = 4a^2 \langle \cos(\theta - \theta_\ell)^2 \rangle$ and its normalized version:

$$g(\theta) = \frac{G(\theta)}{\int_{-\pi}^{\pi} G(\theta)\, \mathrm{d}\theta}$$

The $g(\theta)$ function interprets as the probability to find a neighbor particle at distance $2a$ in the θ direction. The minimum of g is reached at a specific angle, denoted as θ_e and called the depletion angle. Note that, as $\langle \boldsymbol{\ell} \otimes \boldsymbol{\ell} \rangle = \exp(-c\boldsymbol{\gamma}_e)$, the depletion angle is associated to the eigenvector of the largest eigenvalue of $\boldsymbol{\gamma}_e$.

Fig. 11 compares, for various volume fraction, the model prediction of both the depletion angle and the pair distribution with experimental data were presented in [Bla11], Figs. 5.9 to 5.11. For $\phi \leqslant 0.3$ we use the value in steady state produced by the computations done to make Fig. 4. For $\phi < 0.3$ we do a start-up with an imposed shear rate as it is done in [Bla11, ch. 5], using parameters shown in table 1 and $\mu = 0.7$, $n = 2/3$, $\lambda_d = 10^{-4}$. Also, λ, K_e and K_p are extrapolated from the law exposed in Fig. 6. The experiment data and the numerical results were normalized in order to have the same mean. The values of the shear rate are from [Bla11], Table 5.1.

5 Discussion and conclusion

The proposed model could be completely characterized by a simple shear flow experiment, providing either the particle pressure is imposed, as in [BGP11] or the difference of normal stresses is measured, as in [ZHLJ00]. As a preliminary conclusion, this model should be potentially as efficient as the suspension balance model. Its true tensorial formulation also introduces additional important features: anisotropy and a time scale for clusters of particles to relax. Future work will consider more complex flows, such as Couette flows in large gap, with particle migration and shear banding.

A Resolution for simple shear flows

A.1 Explicit resolution

For simplifying the notations, we omit in this section the dependences in ϕ and denote simply G instead of $G(\phi)$. Let $\boldsymbol{u}(x,y,z) = (u_x(y),0,0)$ be the velocity in the stationary regime: accordingly to notations used in experimental papers, such as [ZHLJ00], the x axis is in the flow direction and the y axis in the direction of the gradient $\nabla = (0,\partial_y,0)$. Let $\dot\gamma = u_x'(y)$ that is supposed to be constant. We focus on the stationary shear flow and the damage is supposed to be zero, i.e. no contacts are loss. The constitutive equation of the elastoviscoplastic model writes for a stationary shear flow (see [Sar16], section 4.4):

$$
\begin{aligned}
A\gamma_{e,yy} &= 0 && \text{(10a)}\\
-2\dot\gamma\gamma_{e,xy} + A\gamma_{e,xx} &= 0 && \text{(10b)}\\
-\dot\gamma\gamma_{e,yy} + A\gamma_{e,xy} &= \dot\gamma && \text{(10c)}
\end{aligned}
$$

Note that, from [Sar16], section 4.4, we have swapped the x and y coordinates, in order to be consistent with notations used in experimental papers. We have set for convenience:

$$
A = \frac{1}{\lambda}\max\left(0, \frac{|\mathrm{dev}(\boldsymbol{\gamma}_e)| - \mu\,\mathrm{tr}(\boldsymbol{\gamma}_e)/3}{|\mathrm{dev}(\boldsymbol{\gamma}_e)|^n}\right)^{\frac{1}{n}}
$$

When $A = 0$, we get from (10c) the relation $\dot\gamma\gamma_{e,xy} = 0$ and then $\dot\gamma = 0$ and the particle deformation tensor $\boldsymbol{\gamma}_e$ is undetermined, assuming it satisfies $A = 0$: this is the solid rigid behavior. Next, we assume $A \neq 0$. First, from (10a), we get $\gamma_{e,yy} = 0$. Next, multiplying (10c) by $\gamma_{e,xx}$, ten (10b) by $\gamma_{e,xy}$, and subtracting, we obtain, as $\dot\gamma \neq 0$:

$$
\gamma_{e,xx} = 2\gamma_{e,xy}^2 \qquad \text{(11a)}
$$

Note that, after replacing from (11a) $\gamma_{e,xx}$ by its expression in (10c), we will provide a relation between $\gamma_{e,xy}$ and $\dot\gamma$. We have just to expand first A as an expression involving $\gamma_{e,xy}$ only:

$$
\begin{aligned}
\mathrm{tr}(\boldsymbol{\gamma}_e) &= \gamma_{e,xx} = 2\gamma_{e,xy}^2\\
|\mathrm{dev}(\boldsymbol{\gamma}_e)| &= \left(\gamma_{e,xy}^2 + \frac{\gamma_{e,xx}^2}{3}\right)^{1/2} = \gamma_{e,xy}\left(1 + \frac{4\gamma_{e,xy}^2}{3}\right)^{1/2}\\
\lambda A &= \frac{(|\mathrm{dev}(\boldsymbol{\gamma}_e)| - \mu\,\mathrm{tr}(\boldsymbol{\gamma}_e)/3)^{1/n}}{|\mathrm{dev}(\boldsymbol{\gamma}_e)|}\\
&= \gamma_{e,xy}^{-1+1/n}\left(\left(1 + \frac{4\gamma_{e,xy}^2}{3}\right)^{1/2} - \frac{2\mu\gamma_{e,xy}}{3}\right)^{1/n}\left(1 + \frac{4\gamma_{e,xy}^2}{3}\right)^{-1/2}
\end{aligned}
$$

Without loss of generality, we assume $\dot\gamma > 0$ and $\gamma_{e,xy} > 0$. Replacing in (10c), we obtain an explicit expression for $\lambda\dot\gamma$ in terms of $\gamma_{e,xy}$ only:

$$
\lambda\dot\gamma = f_{n,\mu}(\gamma_{e,xy}) \qquad \text{(11b)}
$$

where the function $f_{n,\mu}$ is defined for all $\gamma_{e,xy} \geqslant 0$ by

$$
f_{n,\mu}(Y) = \gamma_{e,xy}^{1/n}\left(\left(1 + \frac{4}{3}\gamma_{e,xy}^2\right)^{1/2} - \frac{2\mu}{3}\gamma_{e,xy}\right)^{1/n}\left(1 + \frac{4}{3}\gamma_{e,xy}^2\right)^{-1/2}
$$

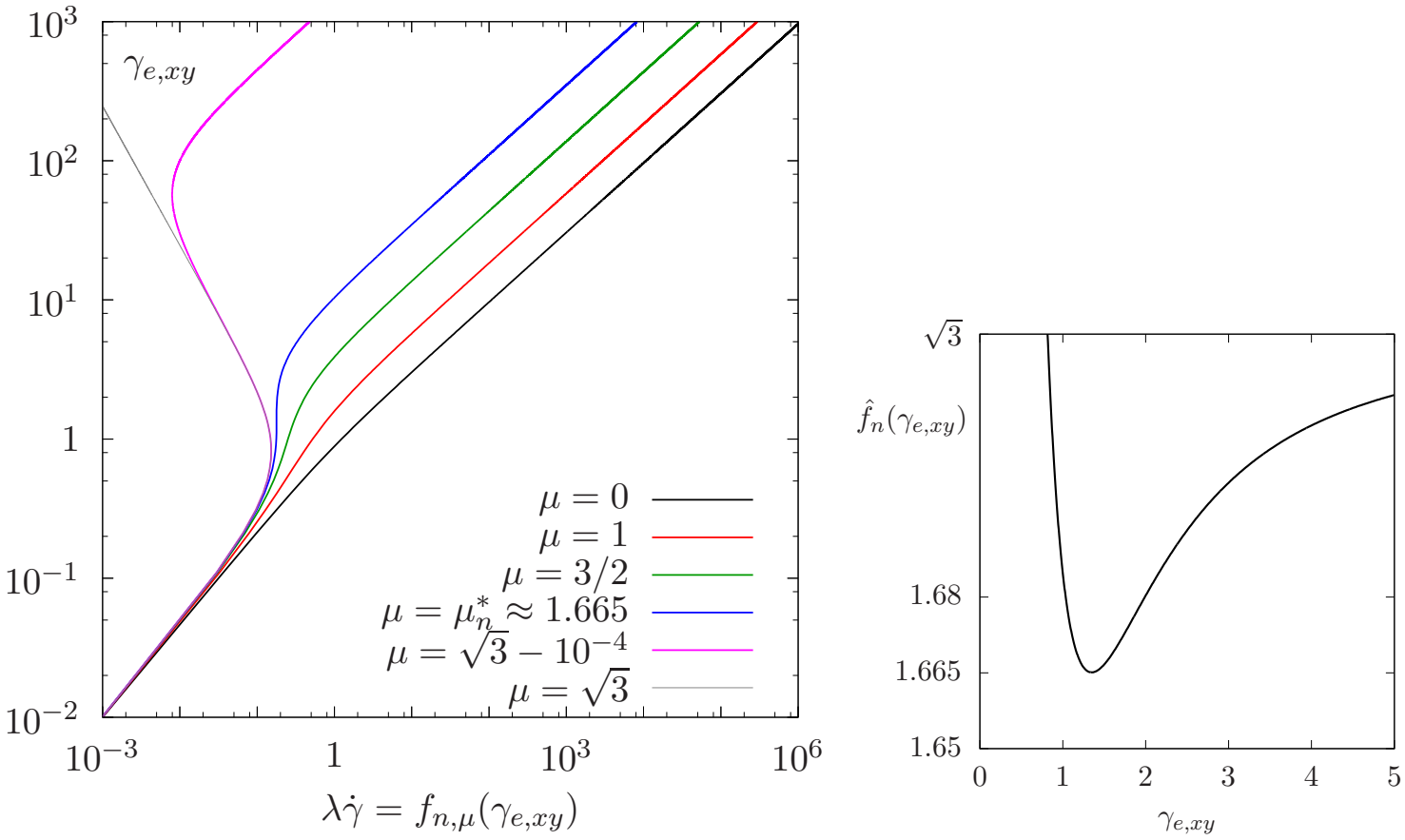

Figure 12: (left) The characteristic function $f_{n,\mu}$ when $n = 2/3$. (right) Computing μ_n^*.

The first factor under the $1/n$ is positive when

$$3 + 4(1-\mu)\gamma_{e,xy}^2 \;\geqslant\; 0$$

When $\mu \leqslant 1$ this condition is satisfied for all $\gamma_{e,xy}$. When $\mu > 1$ this requires $\gamma_{e,xy} \leqslant \sqrt{4(\mu-1)/3}$ and the solution does not exists for large $\gamma_{e,xy}$. Thus, we assume $\mu \leqslant 1$.

Large shear rate regime – When $\gamma_{e,xy}$ becomes large, we have $f_{n,\mu}(\gamma_{e,xy}) \approx c_{n,\mu}\gamma_{e,xy}^{2/n-1}$ with $c_{n,\mu} = (\sqrt{3}/2)^{1-1/n}(1-\mu/\sqrt{3})^{1/n}$. For the function $f_{n,\mu}$ to be strictly increasing when $\gamma_{e,xy} \to +\infty$, we need $c_{n,\mu} > 0$ or equivalently $0 \leqslant \mu < \sqrt{3}$. Then $\lambda\dot\gamma \approx c_{n,\mu}\gamma_{e,xy}^{2/n-1}$ or equivalently $\gamma_{e,xy} \approx (\lambda\dot\gamma/c_{n,\mu})^{n/(2-n)}$. From (11a) we get $\gamma_{e,xx} \approx 2c_{n,\mu}^{-2n/(2-n)}(\lambda\dot\gamma)^{2n/(2-n)}$. In terms of the particle stress $\boldsymbol{\tau} = G\boldsymbol{\gamma}_e$, we get $\tau_{xy} \approx c_1\dot\gamma^{n/(2-n)}$ and $\tau_{xx} \approx c_2\dot\gamma^{2n/(2-n)}$ with c_1 and c_2 independent of $\dot\gamma$. Experimental observations [ZHLJ00,BPG11] showed that the normal stress difference N_1, that coincides here with τ_{xx}, is proportional to $|\dot\gamma|$. This leads to choose $n = 2/3$ for applications. With the choice $n = 2/3$, at large shear rate, τ_{xy} behaves as $\dot\gamma^{1/2}$ and N_1 behaves as $\dot\gamma$.

Small shear rate regime – Conversely, observe that, when $\gamma_{e,xy}$ is small, we have $f_{n,\mu}(\gamma_{e,xy}) \approx \gamma_{e,xy}^{1/n}$. Then $\gamma_{e,xy} \approx (\lambda\dot\gamma)^n$ and $\gamma_{e,xx} \approx 2(\lambda\dot\gamma)^{2n}$. Recall that $\lambda^n = K_e/G$. In terms of the particle stress, we get $\tau_{xy} \approx K_e\dot\gamma^n$ and $\tau_{xx} \approx 2K_e^2G^{-1}\dot\gamma^n$. With the choice $n = 2/3$, at small shear rate, τ_{xy} behaves as $\dot\gamma^{2/3}$ and $N_1 = \tau_{xx}$ behaves as $\dot\gamma^{4/3}$. From Fig. 12.left, we observe that this flow regime is satisfied for $\lambda\dot\gamma$ smaller than 10^{-2}. In most experiments with suspensions, λ is of about 0.1 s to 1 s seconds typical $\dot\gamma$ larger than 0.1 s^{-1}, this flow regime is not clearly observed.

Summary of flow regimes – Notice from (3) that σ_{xy} has an additional viscous term with the $\eta(\phi,\dot\gamma)$ viscosity. Assuming for simplicity that $\eta(\phi,\dot\gamma)$ is independent of $\dot\gamma$,. with the choice $n = 2/3$, σ_{xy} has three

regimes: $\dot\gamma^{2/3}$ at small shear rate, $\dot\gamma^{1/2}$ at intermediate shear rate and $\dot\gamma$ at high shear rate. Conversely, the apparent viscosity behaves as $\dot\gamma^{-1/3}$ at small shear rate, $\dot\gamma^{-1/2}$ at intermediate shear rate and as a constant at high shear rate (see Fig. 13.left). Also, N_1 behaves $\dot\gamma^{4/3}$ at small shear rate, and $\dot\gamma$ at high shear rate (see Fig. 13.right). See [ZHLJ00], Fig. 7 and 10 for these flow regimes.

Exact resolution – The equation $\lambda\dot\gamma = f_{n,\mu}(\gamma_{e,xy})$ can be solved, assuming that $f_{n,\mu}$ is strictly increasing, at least for μ sufficiently small, as shown on Fig. 12. Thus, let us study its derivative:

$$\begin{aligned} f'_{n,\mu}(\gamma_{e,xy}) &= \frac{1}{3^{1/(2n)}n}\gamma_{e,xy}^{1/n-1}\left(3+4\gamma_{e,xy}^2\right)^{-3/2} \\ &\quad\times\left\{\left(3+4\gamma_{e,xy}^2\right)^{1/2}-\frac{2}{\sqrt{3}}\mu\gamma_{e,xy}\right\}^{1/n-1} \\ &\quad\times\left\{\sqrt{3}\left(3+4\gamma_{e,xy}^2\right)^{1/2}\left[4(2-n)\gamma_{e,xy}^2+3\right]-4\mu\gamma_{e,xy}\left[2\left(2-n\right)\gamma_{e,xy}^2+3\right]\right\} \end{aligned}$$

Assuming $\mu\in[0,\sqrt{3}[$, all the factors are positive except perhaps the last one.

$$\begin{aligned} &\sqrt{3}\left(3+4\gamma_{e,xy}^2\right)^{1/2}\left[4(2-n)\gamma_{e,xy}^2+3\right] \;\geqslant\; 4\mu\gamma_{e,xy}\left[2\left(2-n\right)\gamma_{e,xy}^2+3\right],\quad\forall\gamma_{e,xy}\geqslant 0 \\ \iff\quad &\mu\leqslant\mu_n^* = \min_{\gamma_{e,xy}\geqslant 0}\hat f_n(\gamma_{e,xy}) \text{ with } \hat f_n(\gamma_{e,xy}) = \frac{\sqrt{3}\left(3+4\gamma_{e,xy}^2\right)^{1/2}\left[4(2-n)\gamma_{e,xy}^2+3\right]}{12\gamma_{e,xy}\left[2\left(2-n\right)\gamma_{e,xy}^2+3\right]} \end{aligned}$$

Fig. 12 represents the characteristic function $f_{n,\mu}$ and the evaluation of $\mu_n^* \approx= 1.665$ when $n = 2/3$. Observe that when $\mu\in[0,\mu_n^*]$, then $f_{n,\mu}$ is strictly increasing and invertible for all $\gamma_{e,xy}\geqslant 0$. As $f_{n,\mu}$ is differentiable, its inverse i$f_{n,\mu}^{-1}$ can be efficiently computed by a Newton method, up to machine precision, so its computation is considered as exact.

A.2 Imposing both volume fraction and shear rate

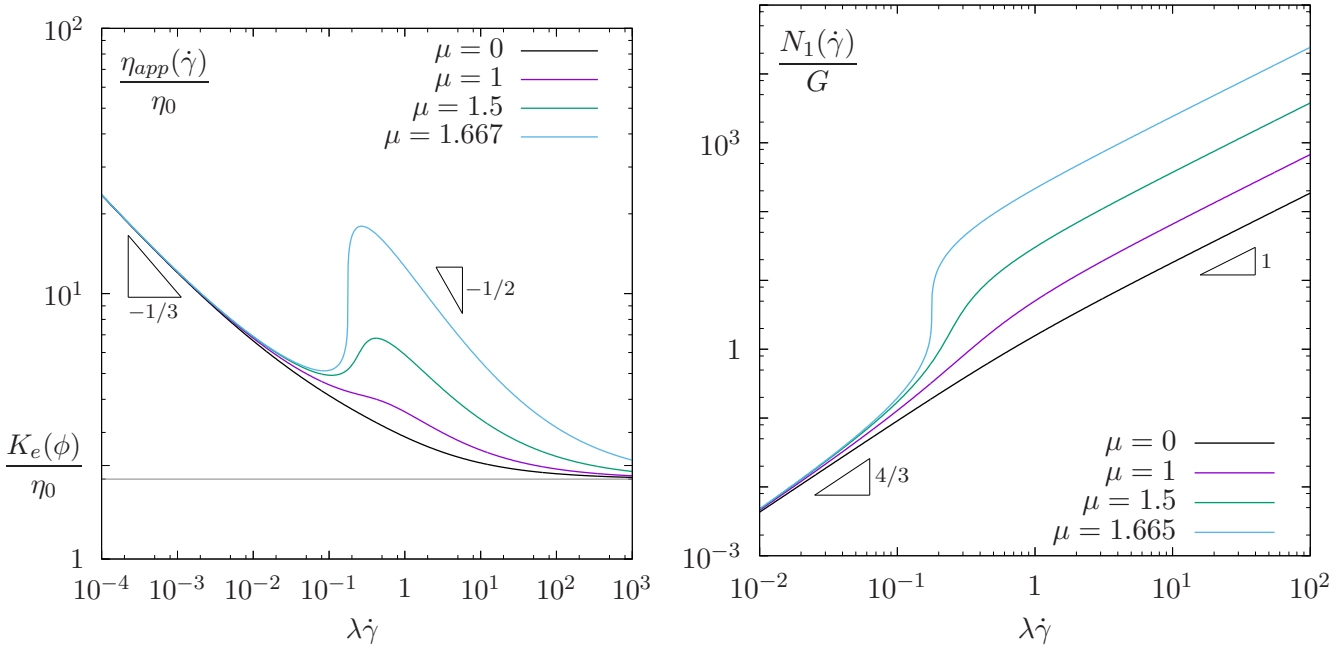

Figure 13: (left) Apparent viscosity ; (right) Normal stress ($n = 2/3$, $K_e = 1$, $G = 1$, $\bar\eta_{\text{app}} = 2$).

From (11b)-(11a), When both the volume fraction ϕ and the shear rate $\dot\gamma$ are imposed, the solution writes:

$$
\begin{aligned}
\tau_{xy} &= G\, f_{n,\mu}^{-1}(\lambda\dot\gamma) \\
\sigma_{xx} &= \tau_{xx} = 2G\,\left(f_{n,\mu}^{-1}(\lambda\dot\gamma)\right)^2 && \text{(12a)}\\
\sigma_{xy} &= \eta(\dot\gamma)\dot\gamma + G\, f_{n,\mu}^{-1}(\lambda\dot\gamma) && \text{(12b)}\\
\eta_{\text{app}}(\dot\gamma) &= \eta(\dot\gamma) + G f_{n,\mu}^{-1}(\lambda\dot\gamma)\,\dot\gamma^{-1} && \text{(12c)}
\end{aligned}
$$

Notice that $\sigma_{yy} = \sigma_{zz} = 0$ and thus $N_2 = 0$ and $N_1 - N_2 = \tau_{xx}$. The solution is represented on Fig. 13 for various friction coefficient values. Observe that the apparent viscosity is monotonically decreasing when $\mu = 0$ i.e. shear-thinning. This property is loss for sufficiently large μ e.g. $\mu = 1.5$: the apparent viscosity presents a region of shear-thickening at small shear rate and then, for large shear rate, the apparent viscosity is decreasing. Conversely, N_1 presents a region where there is a rapid growth. From experimental observations, we have $\mu \approx 0.7$: in that case, the main behavior is almost smooth.

Using the development of $f_{n,\mu}$ for large $\dot\gamma$ when $n = 2/3$, we get:

$$
\begin{aligned}
\tau_{xy} &= G\left(\frac{\lambda\dot\gamma}{c_{2/3,\mu}}\right)^{1/2} && \text{(13a)}\\
\tau_{xx} &= 2G\,\frac{\lambda\dot\gamma}{c_{2/3,\mu}} && \text{(13b)}
\end{aligned}
$$

A.3 Imposing both particle pressure and shear stress

As the particle pressure $p_p = \mathrm{tr}(\boldsymbol{\tau})/3 = \tau_{xx}$ is imposed, the normal stress is known: $\tau_{xx} = 3p_p$. Then, from (2) we get $\gamma_{e,xx} = 3p_p/G(\phi)$ and, from (11a), we obtain $\gamma_{e,xy} = \sqrt{3p_p/(2G(\phi))}$. From (11b), and since $G = K_e/\lambda^n$, we get

$$\lambda(\phi)\dot{\gamma} \;=\; f_{n,\mu}\left(\left(\frac{3p_p\lambda(\phi)^n}{2K_e(\phi)}\right)^{1/2}\right) \;\Longleftrightarrow\; K_e(\phi) \;=\; \frac{3p_p\,\lambda(\phi)^n}{2\left\{f_{n,\mu}^{-1}\left(\lambda(\phi)\,\dot{\gamma}\right)\right\}^2} \tag{14}$$

Relation between I_v and ϕ – Following [BGP11], we introduce the dimensionless number $I_v = \eta_0\dot{\gamma}/p_p$ and the previous equation rewrites in terms of I_v instead of $\dot{\gamma}$ as:

$$I_v \;=\; \frac{\eta_0}{p_p\,\lambda(\phi)} f_{n,\mu}\left(\left(\frac{3p_p\,\lambda(\phi)^n}{2K_e(\phi)}\right)^{1/2}\right) \tag{15}$$

It expresses I_v versus ϕ where p_p is imposed and the material functions $\lambda(\phi)$ and $K_e(\phi)$ are given by (7a)-(7b).

Relation between σ_{xy} and $\dot{\gamma}$ – From (3), we obtain the shear stress :

$$\sigma_{xy} \;=\; K_p(\phi)\dot{\gamma}^{m_p(\phi)} + \tau_{xy} \;=\; K_p(\phi)\dot{\gamma}^{m_p(\phi)} + \left(\frac{3p_p\lambda(\phi)^n}{2K_e(\phi)}\right)^{1/2} \tag{16}$$

Next, it remains to replace in the previous expression ϕ by an expression in terms of $\dot{\gamma}$. There are two ways to find such an expression. The first way bases on (15). Note that I_v expresses simply in terms of $\dot{\gamma}$ and p_p, thus (15) is equivalent to an expression of $\dot{\gamma}$ in terms of ϕ, as p_p is given, and is represented on Fig. 8.left. It could be inverted, e.g. by a Newton method, in order to obtain ϕ as an expression in terms of $\dot{\gamma}$. The second way bases on the empirical relation (9), which simpler and sufficiently accurate for our purpose, as shown on Fig. 8.left. By one of these ways, (16) reduces to an expression of σ_{xy} in terms of $\dot{\gamma}$.

References

[AJGG03] M. Aubouy, Y. Jiang, J. A. Glazier, and F. Graner. A texture tensor to quantify deformations. *Granular Matter*, 5(2):67–70, 2003.

[BGP11] F. Boyer, É. Guazzelli, and O. Pouliquen. Unifying suspension and granular rheology. *Phys. Rev. Lett.*, 107(18):188301, 2011.

[Bla11] F. Blanc. *Rhéologie et microstructure des suspensions concentrées non browniennes*. PhD thesis, Université Nice Sophia Antipolis, 2011.

[BLMP13] F. Blanc, E. Lemaire, A. Meunier, and F. Peters. Microstructure in sheared non-Brownian concentrated suspensions. *J. Rheol.*, 57(1):273–292, 2013.

[BPG11] F. Boyer, O. Pouliquen, and É. Guazzelli. Dense suspensions in rotating-rod flows: normal stresses and particle migration. *J. Fluid Mech.*, 686:5–25, 2011.

[BPL11a] F. Blanc, F. Peters, and E. Lemaire. Experimental signature of the pair trajectories of rough spheres in the shear-induced microstructure in noncolloidal suspensions. *Phys. Rev. Lett.*, 107(20):208302, 2011.

[BPL11b] F. Blanc, F. Peters, and E. Lemaire. Local transient rheological behavior of concentrated suspensions. *J. Rheol.*, 55(4):835–854, 2011.

[DGM+09] A. Deboeuf, G. Gauthier, J. Martin, Y. Yurkovetsky, and J. F. Morris. Particle pressure in a sheared suspension: a bridge from osmosis to granular dilatancy. *Physical review letters*, 102(10):108301, 2009.

[DP52] D. C. Drucker and W. Prager. Soil mechanics and plastic analysis or limit design. *Quart. Appl. Math.*, 10(2):157–165, 1952.

[EBH11] J. W. Eaton, D. Bateman, and S. Hauberg. *Octave: A high-level interactive language for numerical computations*. Free software fundation, 2011. http://www.gnu.org/software/octave.

[Ein06] A. Einstein. Eine neue bestimmung der moleküldimensionen. *Ann. Phys. ser. 4*, 19:289–306, 1906.

[GMA80] F. Gadala-Maria and A. Acrivos. Shear-induced structure in a concentrated suspension of solid spheres. *J. Rheol.*, 24(6):799–814, 1980.

[HB26] W. H. Herschel and T. Bulkley. Measurement of consistency as applied to rubber-benzene solutions. *Proc. Amer. Soc. Testing Material*, 26(2):621–633, 1926.

[KD59] I. M. Krieger and T. J. Dougherty. A mechanism for non-newtonian flow in suspensions of rigid spheres. *Trans. Soc. Rheol.*, 3(1):137–152, 1959.

[KPGM02] V. G. Kolli, E. J. Pollauf, and F. Gadala-Maria. Transient normal stress response in a concentrated suspension of spherical particles. *J. Rheol.*, 46(1):321–334, 2002.

[Lar99] R. L. Larson. *The structure and rheology of complex fluids*. Oxford University Press, UK, 1999.

[LWD+15] R. Lehoucq, J. Weiss, B. Dubrulle, A. Amon, A. le Bouil, J. Crassous, D. Amitrano, and F. Graner. Analysis of image vs. position, scale and direction reveals pattern texture anisotropy. *Frontiers in Physics*, 2:84, 2015.

[Mau92] G. A. Maugin. *The thermomechanics of plasticity and fracture*. Cambridge University Press, UK, 1992.

[MB99] J. F Morris and F. Boulay. Curvilinear flows of noncolloidal suspensions: the role of normal stresses. *J. Rheol.*, 43(5):1213–1237, 1999.

[MM06] R. M. Miller and J. F. Morris. Normal stress-driven migration and axial development in pressure-driven flow of concentrated suspensions. *J. Non-Newt. Fluid Mech.*, 135(2):149–165, 2006.

[NB94] P. R. Nott and J. F. Brady. Pressure-driven flow of suspensions: simulation and theory. *J. Fluid Mech.*, 275:157–199, 1994.

[NSH+02] T. Narumi, H. See, Y. Honma, T. Hasegawa, T. Takahashi, and N. Phan-Thien. Transient response of concentrated suspensions after shear reversal. *J. Rheol.*, 46(1):295–305, 2002.

[RH93] K. Radhakrishnan and A. C. Hindmarsh. Description and use of LSODE, the Livermore solver for ordinary differential equations. Technical Report UCRL-ID-113855, LLNL, 1993.

[Sar07] P. Saramito. A new constitutive equation for elastoviscoplastic fluid flows. *J. Non-Newt. Fluid Mech.*, 145(1):1–14, 2007.

[Sar09] P. Saramito. A new elastoviscoplastic model based on the Herschel-Bulkley viscoplasticity. *J. Non-Newt. Fluid Mech.*, 158(1–3):154–161, 2009.

[Sar16] P. Saramito. *Complex fluids: modelling and algorithms*. Springer, 2016.

[SB02] A. Sierou and J. F. Brady. Rheology and microstructure in concentrated noncolloidal suspensions. *J. Rheol.*, 46(5):1031–1056, 2002.

[WK10] T. Williams and C. Keley. `gnuplot`: an interactive program, 2010. http://www.gnuplot.info.

[YM08] Y. Yurkovetsky and J. F. Morris. Particle pressure in sheared Brownian suspensions. *J. Rheology*, 52(1):141–164, 2008.

[ZHLJ00] I. E. Zarraga, D. A. Hill, and D. T. Leighton Jr. The characterization of the total stress of concentrated suspensions of noncolloidal spheres in Newtonian fluids. *J. Rheol.*, 44(2):185–220, 2000.